Final published version of this article: **The Journal of Physical Chemistry C**,
Cite: J. Phys. Chem. C 2022, 126, 16, 7076–7085
Available online: 15 April 2022
DOI: https://doi.org/10.1021/acs.jpcc.1c10053

Electronic structure of $V_xTi_{1-x}Se_2$ solid solutions with the $(V,Ti)Se_2$ structural fragments

A.S. Shkvarin[1*], A.I. Merentsov[1], M.S. Postnikov[1], Yu.M. Yarmoshenko[1], E.G. Shkvarina[1], E.A. Suslov[1], A.Yu. Kuznetsova[1,2], I. Píš[3,4], S. Nappini[4], F. Bondino[4], P. Moras[5], P.M. Sheverdyaeva[5], E. Betz-Guttner [4], A.N. Titov[1]

[1]M.N. Miheev Institute of Metal Physics of Ural Branch of Russian Academy of Sciences, 620990 Ekaterinburg, Russia

[2]Ural Federal University, 620089 Ekaterinburg, Russia

[3]Elettra-Sincrotrone Trieste S.C.p.A, S.S. 14, km 163.5, 34149 Basovizza, Trieste, Italy

[4]IOM-CNR, Laboratorio TASC, S.S. 14-km 163.5, 34149 Basovizza, Trieste, Italy

[5]Istituto di Struttura della Materia-CNR (ISM-CNR), SS 14, Km 163,5, 34149, Trieste, Italy

[*]Email: shkvarin@imp.uran.ru

Abstract

The equilibrium boundary for the layered $V_xTi_{1-x}Se_2$ solid solution was determined according to a set of experimental data of synchrotron radiation X-ray photoelectron spectroscopy and electromotive force of the $Li|Li^+|V_xTi_{1-x}Se_2$ electrochemical cells. This boundary appears to be 20 mol.% of V (x = 0.2). The formation of the VSe_2 structural fragments, which are tightly bounded with $V_xTi_{1-x}Se_2$ layers, appears at x > 0.2. A combined analysis of the Fermi-surface maps and the atomic force microscopy (AFM) images reveals that the (001) planes in VSe_2 and $V_xTi_{1-x}Se_2$ structural fragments are parallel to each other. At the same time, these fragments demonstrate turbostratic disordering within the basal plane. The formation of such pseudo-homogeneous materials is associated with the contribution of the free surface energy, that is relatively high in the quasi-two-dimensional materials.

Introduction

Layered quasi-two-dimensional materials based on titanium dichalcogenides have been attracting attention for several decades. Phenomena such as superconductivity[1], charge density waves[2], and spin polarization[3] are typical for these materials. Their crystal lattice consists of Ch-Ti-Ch layers (Ch = S, Se, Te), which are usually called "sandwich". In the "sandwich" there is a strong interaction between the atoms, whereas the adjacent sandwich layers are held together by relatively weak van der Waals forces. This makes it possible to intercalate different atoms or molecules[4] into the interlayer space (see figure 1).

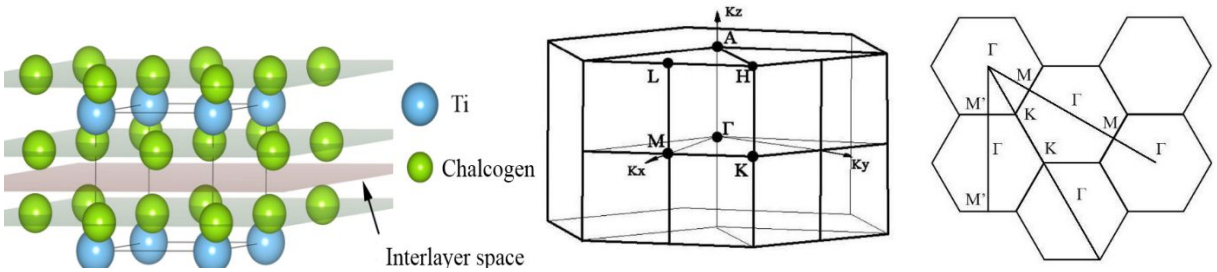

Figure 1. A fragment of the $TiCh_2$ crystal structure (left panel). The 1st Brillouin zone for $TiCh_2$ (middle panel). Representation of the highly symmetric directions in the k-space (right panel).

$TiCh_2$ is one of the most promising cathode materials for lithium batteries[5–10]. Batteries with electrodes based on $TiCh_2$, VCh_2 (Ch = S, Se), and their solid solutions are already widely used. An amazing property is a huge difference in the kinetics of electrode processes in the solid solutions compared to the pure $TiCh_2$ and VCh_2 (Ch = S, Se) host compounds[11,12]. Since the Li atoms occupy the same crystallographic sites in the solid solutions as in the host compounds, it seems difficult to explain the origin of the difference in the diffusion mobility of Li in solid solutions. On the other hand, the previously discovered formation of mesoscopic structural fragments (SF) (for example, in the $Cr_xTi_{1-x}Se_2$ or $TiSe_xS_{2-x}$ solutions) could explain this unusual phenomenon[13,14]. The formation of structural fragments was suggested also for $V_xTi_{1-x}Se_2$ [15]. However, the question about the conjugation character of these SFs remains. For example, when SFs are present, the change of the lattice parameters is almost linear with the metal concentration. This indicates the strong interaction between these SFs and, probably, their coherent conjugation. In this work, we study the origin of the conjugation of SFs.

The SFs are not formed at low concentrations of the substituent component in $V_xTi_{1-x}Se_2$ due to a large entropy contribution. To determine the vanadium concentration, at which the SFs are being formed in $V_xTi_{1-x}Se_2$, we measured the electromotive force (EMF) of $Li|Li^+|V_xTi_{1-x}Se_2$ electrochemical cells relative to the metallic lithium.

The electrochemical properties of the lithium battery system with $V_xTi_{1-x}Se_2$ cathode were investigated previously[15]. However, only the compounds with $x < 0.5$ were studied. For these compounds the physical properties[16,17], crystal structure[16,18], and electronic structure[18,19] have been studied. The host compounds $TiSe_2$ and VSe_2 have been studied for a long time[20,21,30,22–29]. There is a slight deviation from Vegard's law in the V concentration dependence of the lattice parameters for $V_xTi_{1-x}Se_2$ [16,18].

In the current work we focused on $V_xTi_{1-x}Se_2$ system, where the vanadium substituent concentration ($x = 0.5, 0.73$) is high enough for the formation of the structural fragments. Synchrotron radiation X-ray photoelectron spectroscopy (XPS), including resonant photoelectron spectroscopy (ResPES), ARPES, and X-ray absorption spectroscopy (XAS) were used to study the electronic structure. These methods were complemented by the AFM and EMF measurements, and first-principle calculations.

Experiment and theory

Polycrystalline $TiSe_2$ and VSe_2 were synthesized in sealed quartz ampoules evacuated to 10^{-5} torr. The synthesis technique was described in details in Ref. [15]. Titanium (after iodine purification, 99.95%), vanadium (99.95%) and selenium (OSCh19-5, 99.999%) were used as starting materials. Polycrystalline $V_xTi_{1-x}Se_2$ compounds were synthesized from preliminary prepared $TiSe_2$ and VSe_2 powders taken in the required stoichiometric ratios in sealed quartz ampoules evacuated to 10^{-5} Torr at a temperature of 800 ˚C for 1 week. Afterwards the obtained material was grinded, pressed into pellets and homogenized at the same conditions. Single crystals of $V_xTi_{1-x}Se_2$ were grown in sealed quartz ampoules evacuated to 10^{-5} Torr using gas-transport reaction technique[31]. The 10 cm length ampule with a previously prepared polycrystalline $V_xTi_{1-x}Se_2$ material was placed into the furnace with a temperature gradient. The temperatures of the hot end and cold end were set to 900 ˚C and 600 ˚C respectively. The single crystals studied in this work grew on the cold end of the ampoule.

The chemical composition of the crystals was determined using EDX technique on an Inspect 1F scanning electron microscope. The results were confirmed by analyzing the intensities of the spectral lines at the XPS experiments.

The XPS, XAS and ResPES spectra were collected from the following single crystals: VSe_2, $V_{0.73}Ti_{0.42}Se_2$, and $V_{0.5}Ti_{0.5}Se_2$. It has been shown in several studies [32–36] that the Se saturation vapor pressure is substantially higher in VSe_2 than in $TiSe_2$. The increase in the Se pressure results in the enrichment of the compound with metal. Therefore, all the $V_xTi_{1-x}Se_2$ compounds with $x > 0.5$ contain superstoichiometric metal. In our previous study,[19] we have shown that the excess of metal in $V_{0.73}Ti_{0.42}Se_2$ is due to the Ti self-intercalation. The spectral data for $TiSe_2$ were reported earlier [37].

The structure and phase purity of the powder $V_xTi_{1-x}Se_2$ samples were checked by X-ray powder diffraction technique (XRD) in the Institute of Metallurgy UrD RAS, CUC "Ural-M" using a Shimadzu XRD 7000 Maxima difractometer (Cu Kα radiation, graphite monochromator). We reported the results on the crystal structure of the substitution $V_xTi_{1-x}Se_2$[18] and intercalation V_xTiSe_2[38] compounds in previous works.

The XPS, XAS and ResPES spectra of $V_xTi_{1-x}Se_2$ were obtained at the BACH beamline [39] at the Elettra synchrotron facility (Trieste, Italy). All samples were cleaved in situ in an ultra high vacuum (UHV) chamber at a pressure lower than 1×10^{-9} Torr. The purity of the surface was confirmed by the absence of oxygen and carbon peaks in the survey spectra. Low energy electron diffraction (LEED) images from the in UHV cleaved samples (see figure S0 in the Supporting Information) confirm the good crystalline quality of the studied crystals. The XPS and ResPES spectra were measured at normal emission with a Scienta R3000 electron energy analyzer. The photoelectron escape depth for these measurements did not exceed 10 Å thus ensuring high surface sensitivity. The total instrumental resolution was 0.2 eV. Binding energies of spectra were calibrated to the Fermi edge measured on a clean Au foil in electrical contact with the samples. The photon energies were calibrated using the difference in the kinetic energy of Au 4f line recorded in the first- and second-order light. The ARPES experiment was performed at the VUV photoemission beamline at Elettra synchrotron facility (Trieste, Italy). The spectra were acquired at a photon energy of E_{exc}= 45 eV with linear polarization in horizontal plane, at a temperature of 9.6 K, using a Scienta R-4000 electron analyzer. The total energy and angular resolution were set to 15 meV and 0.3°, respectively. The used excitation energy E_{exc} = 45 eV corresponds to the point of about 0.25 $k_\perp/k_{\Gamma\text{-}A}$ in the $k_\perp$ direction[40]. Since we are close to the Γ point in the Γ-A direction, we will use for the simplicity of notation the same symbols as for the points in the ΓMK plane (see figure 1).

The first principles calculations were performed using the full potential linearized augmented plane wave (FP-LAPW) approach and the (GGA-PBE)[41] exchange-correlation functional in the ELK software package[42]. Integration over the Brillouin zone was carried out using an 8×8×8 grid of special k points. The self-consistent calculation was finished when the total energy change became less than 0.0001 eV. The calculations were performed on the "Uran" supercomputer at the Institute of Mathematics and Mechanics, Ural division of the Russian Academy of Sciences.

The EMF data were obtained using $Li|Li^+|V_xTi_{1-x}Se_2$ electrochemical cells at a temperature of 25 °C. The measurements were performed in two-contact cells, where metallic lithium (99.9%, Novosibirsk Chemical Concentrates Plant) was a negative and a reference electrode. A 1 M solution of $LiClO_4$ in anhydrous propylene carbonate was used as the electrolyte. The cell assembly and measurements were performed in an argon dry glove box UNILAB MBRAUN (the residual content of water and oxygen was less than 0.1 ppm). The

EMF measurements were performed using a V7-34A voltmeter (impedance input -2·109 Ω) and an Elins P-8S potentiostat.

Result and discussion

XPS

The Se 3d spectra of all samples studied in this work display a single main component at binding energy of 53.2 eV ($3d_{5/2}$) and have the same energy position and similar shape (see figure S1 in Supporting Information). The shape of all the Ti 2p spectra is also nearly the same (figure S1), but the binding energy gradually decreases from 455.67 eV ($2p_{3/2}$) for $TiSe_2$ to 455.29 eV for $V_{0.73}Ti_{0.42}Se_2$ as the V concentration increases. Figure S2 shows the valence band (VB) spectra for the studied compounds. The main features, marked as M, N, Q, and T, are formed by M 3d/S 4p (M = Ti, V) hybridized states. The peak denoted as Se belongs to Se 4s states [37]. The S 3d, Ti 2p core levels and the overall shape of the VB spectra agree well with those reported previously [18].

The VB spectra obtained across the Ti 2p-3d and V 2p-3d resonant excitation [43–47] for $V_{0.5}Ti_{0.5}Se_2$ and $V_{0.73}Ti_{0.42}Se_2$ are shown in figures S3 and S4. The resonant photoemission valence band maps, constant initial state (CIS) spectra (figure S5), as well as the valence band spectra at the maximum resonant enhancement (figure S6) are also in good agreement with results previously reported for similar compounds [18,19]. The qualitative agreement between the current and previous experimental results allows us to expand the conclusions of the current study on the entire $V_xTi_{1-x}Se_2$ system.

Figure 2 shows the V 2p spectra of $V_xTi_{1-x}Se_2$ for V concentrations of $x \geq 0.5$. The energy position of the spectra coincides with that of VSe_2. The V 2p spectrum is shifted towards higher binding energies only for $V_{0.5}Ti_{0.5}Se_2$. At $x > 0.5$ we can consider this system as substitutional Ti doped VSe_2. The V 2p spectra can be fitted with two components, a main one at higher binding energy (peak A) and a second one at lower binding energy (peak B). An increase in the Ti concentration leads to a decrease in the intensity of the B component, which will be discussed later (figure 2 and Table 1).

Table 1. The V 2p binding energy positions and peaks areas of the spectra displayed in figure 2. V $2p_{3/2}$ B component binding energy and relative peak intensity.

Sample	Peak B position, eV	Peak B area/Peak A area
VSe_2	512.27	0.23
$V_{0.73}Ti_{0.42}Se_2$	512.26	0.17
$V_{0.5}Ti_{0.5}Se_2$	512.40	0.16

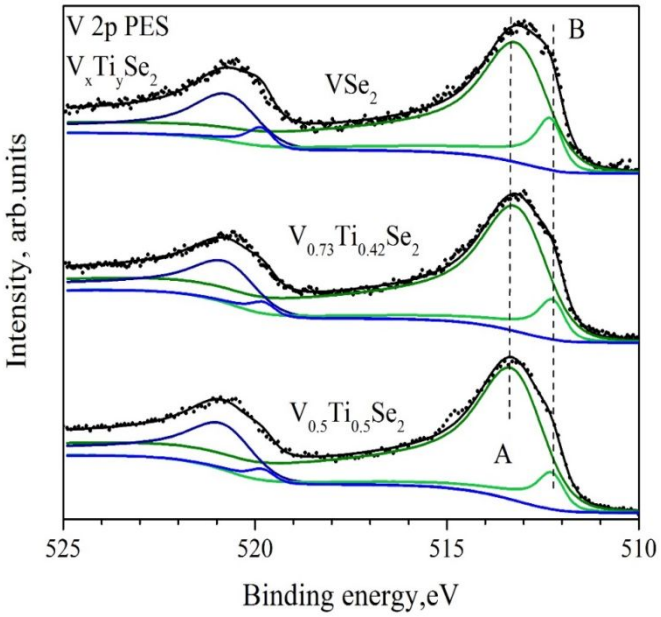

Figure 2. V 2p XPS spectra for $V_xTi_{1-x}Se_2$ recorded at normal emission with photon energy $h\nu$= 602 eV.

The core level spectra provide information about the quality of both the single crystal and the surface. Phase inhomogeneities and surface contamination significantly change the chalcogen core-level spectrum. Therefore, we acquired the core-level XPS spectra for the studied crystals. Firstly, this data confirms good quality of the crystals. Secondly, we see that the crystals studied in the current work belong to the same $V_xTi_{1-x}Se_2$ family as the samples we have studied previously[18].

ARPES

No significant differences were observed in the line shape of the core level spectra for $V_xTi_{1-x}Se_2$ samples as a function of different stoichiometry. However, further insight on the electronic structure of these compounds is obtained by valence band ARPES.

Figure 3 shows the ARPES images for $V_{0.5}Ti_{0.5}Se_2$ and $V_{0.73}Ti_{0.42}Se_2$ along the highly symmetric directions Γ-M, Γ-M', Γ-K.

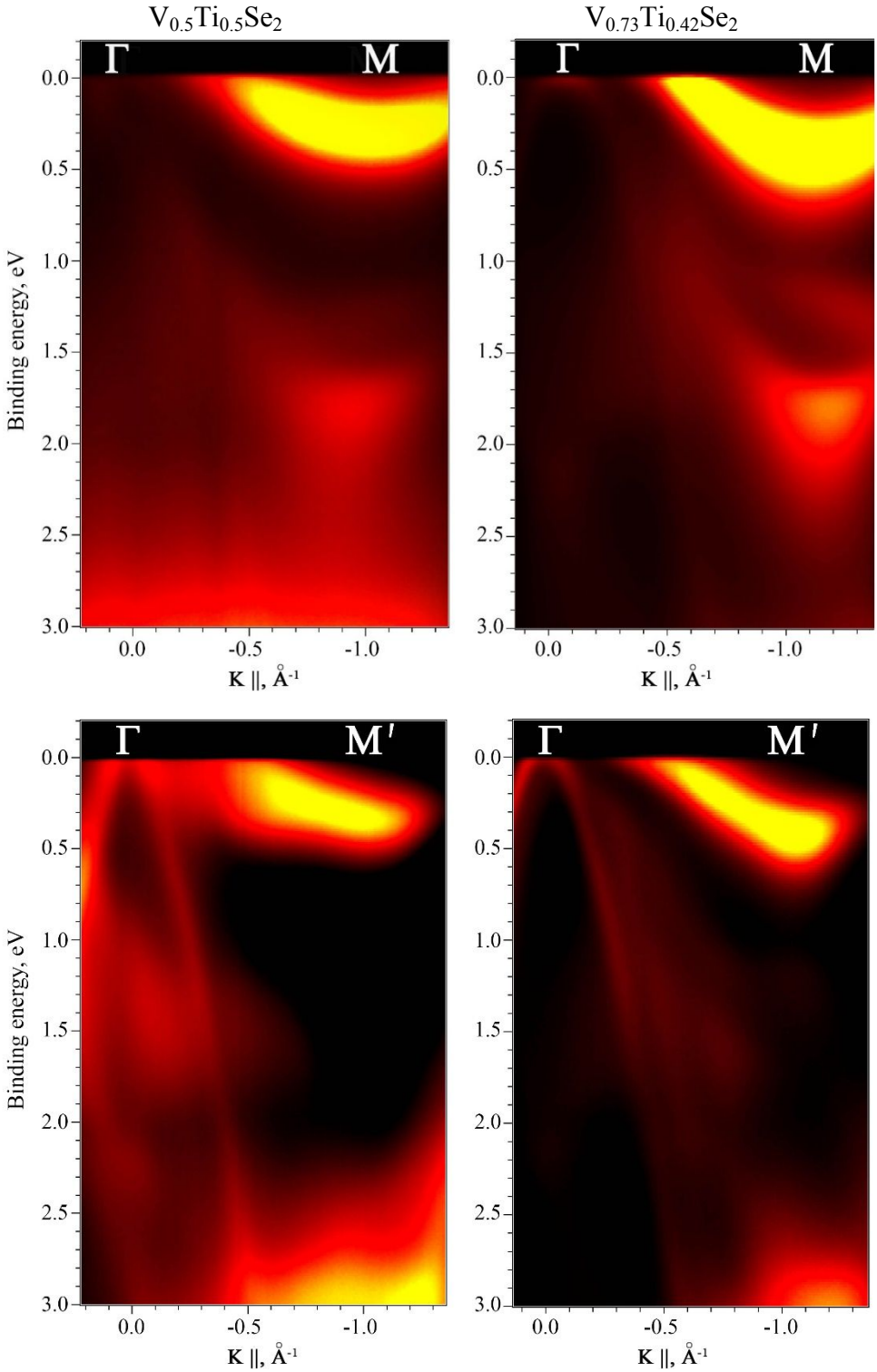
$V_{0.5}Ti_{0.5}Se_2$
$V_{0.73}Ti_{0.42}Se_2$
Γ
M
M′
Binding energy, eV
K ||, Å^{-1}
0.0
0.5
1.0
1.5
2.0
2.5
3.0
-0.5
-1.0

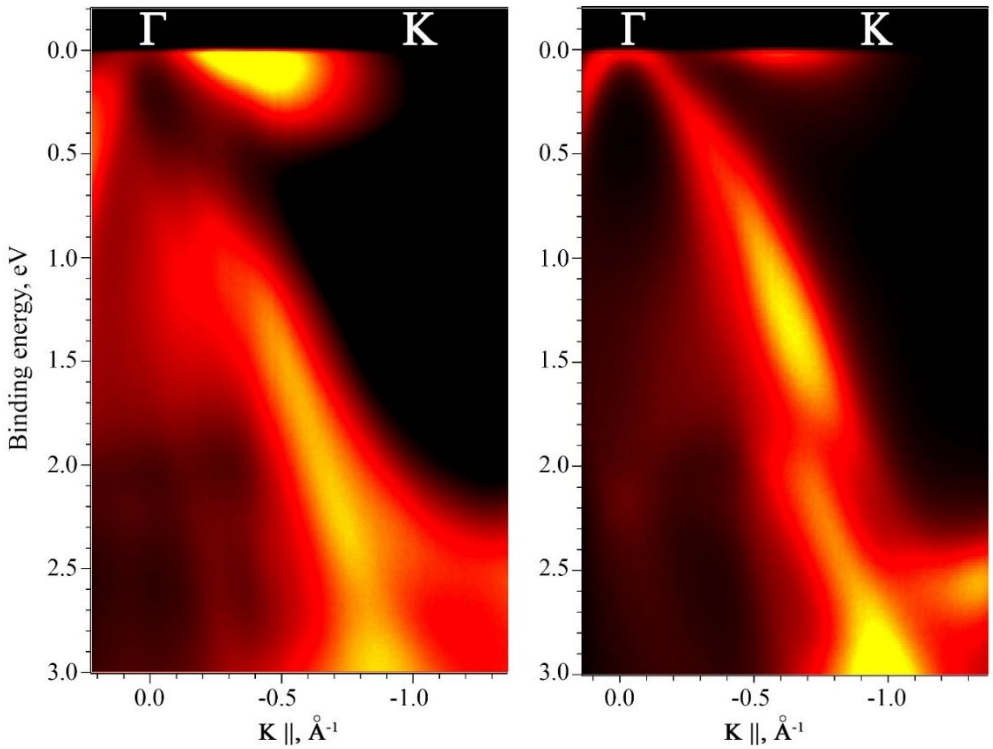

Figure 3. ARPES images for $V_{0.5}Ti_{0.5}Se_2$ and $V_{0.73}Ti_{0.42}Se_2$ along the Γ-M, Γ-M' and Γ-K directions.

The ARPES spectra for $V_{0.5}Ti_{0.5}Se_2$ and $V_{0.73}Ti_{0.42}Se_2$ look similar to those of VSe_2[48]. An expansion of the electron pocket at M point occurs with increasing V concentration. There is an increase in the intensity and binding energy of the bands in the vicinity of the M' point. The most prominent change appears in the band near of the Fermi level in the Γ-K direction (figure 3, lower panel). The band is clearly visible for $V_{0.5}Ti_{0.5}Se_2$, but it is much less pronounced for $V_{0.73}Ti_{0.42}Se_2$. Since the Brillouin zone of the $P\bar{3}m1$ space group has no bands in this point (see figure 4), we can assume that this band appears due to one SF rotated with respect to another one. As the Γ point position is independent from any rotation of the SF, the presence of rotated SF can be evaluated by possible rotations of the M point. Because the intensity of the band in the M point is higher for $V_{0.73}Ti_{0.42}Se_2$ than for $V_{0.5}Ti_{0.5}Se_2$, the intensity of the band located in the intermediate point should be also higher for $V_{0.73}Ti_{0.42}Se_2$. The fact that it is not so indicates that the SFs in $V_{0.5}Ti_{0.5}Se_2$ and $V_{0.73}Ti_{0.42}Se_2$ crystals are rotated at different angles (denoted as α and β in figure 5) with respect to each other as confirmed by constant-energy maps, which are shown in figure 5.

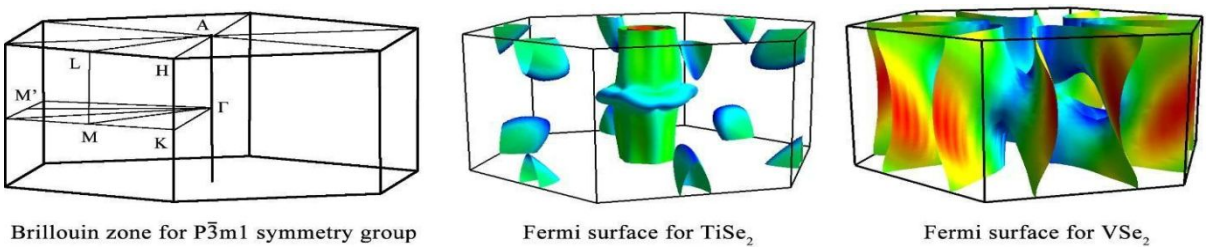

Figure 4. Brillouin zone for $P\bar{3}m1$ space group (left panel), calculated Fermi surface for $TiSe_2$ (central panel) and VSe_2 (right panel).

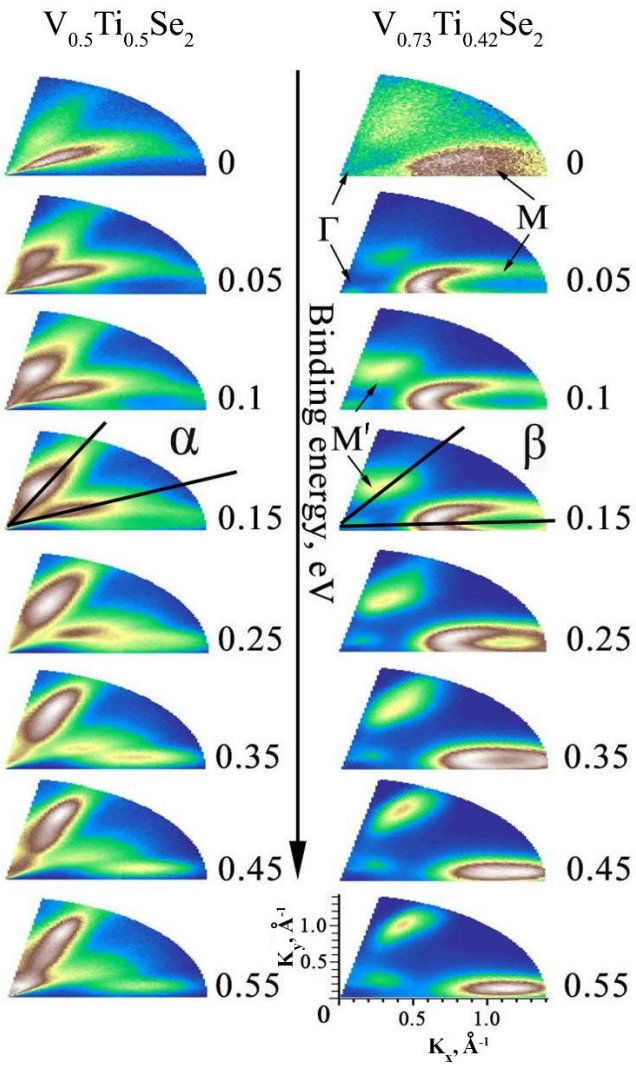

Figure 5. Stack of constant-energy surfaces at indicated binding energies extracted from the ARPES measurements for $V_{0.5}Ti_{0.5}Se_2$ and $V_{0.73}Ti_{0.42}Se_2$.

The ARPES spectra obtained here can be compared with the data reported for 1T-$TiSe_2$ and 1T-VSe_2.[49,50] Because the upper chalcogen layer in the Ch-Ti-Ch "sandwich" is rotated 60° with respect to the lower one, the ARPES spectra for 1T systems differ from each other at the M and M' points. As a result, the electron pockets are clearly visible at the M points with a 120° period, which corresponds to the third-order axis in the $P\bar{3}m1$ space group. The pockets with lower intensity are observed at the M' point.

The electron pockets are clearly distinguishable on the constant-energy surface for $V_{0.5}Ti_{0.5}Se_2$ (figure 5). However, there is a 40° α angle between them, which does not fit the compound symmetry. On the other hand, a 60° β angle between the electron pockets is visible for $V_{0.73}Ti_{0.42}TiSe_2$. The 60° angle belongs to the symmetry elements of the $P\bar{3}m1$ space group, therefore, a 60° relative position of the SFs in $V_{0.73}Ti_{0.42}Se_2$ crystal displays their coherent bounding with each other. This leads to the difference in the intensity of the band located between the Γ and K points (figure 3, lower panel), which is lower for the $V_{0.73}Ti_{0.42}Se_2$ crystal as compared to the $V_{0.5}Ti_{0.5}Se_2$ one. To reveal the reason for this difference, we performed the calculation of the Fermi surface.

Calculation

In this work we consider three substitutional crystal structures with different periodic ordering: a) the formation of (001) Ti planes and (002) V planes (O1); b) the formation of (100) Ti planes and (200) V planes (O2); c) the formation of (1-11) Ti planes and (-11-1) V planes (O3). The modeled crystal structures discussed above are shown in figure 6. However, the calculations cannot be performed for the model which supposes the independent (or dependent) coexistence of the $TiSe_2$ and VSe_2 structural fragments because of a lot of atoms in the modeled crystal structure.

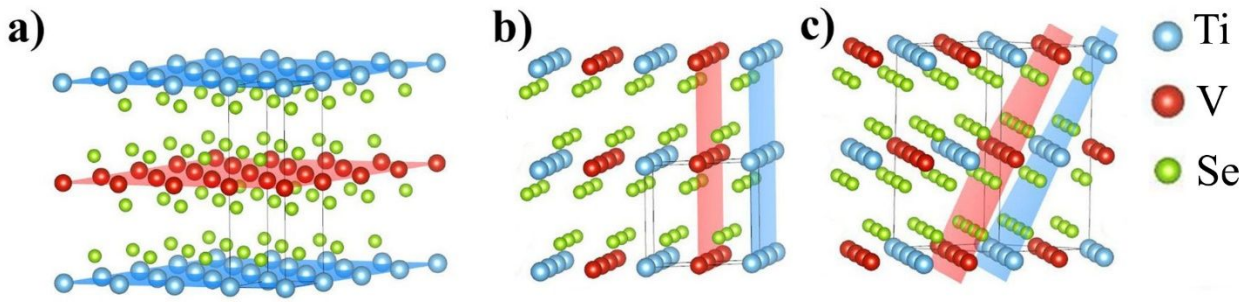

Figure 6. $V_xTi_{1-x}Se_2$ structural models considered for the valence band electronic structure calculations. (a) (001) Ti planes and (002) V planes (O1); (b) (100) Ti planes and (200) V planes (O2); (c) (1-11) Ti planes and (-11-1) V planes (O3).

The calculation was performed for $V_{0.5}Ti_{0.5}Se_2$ for simplicity. The lattice parameters and atomic coordinates were taken from Ref. [18]. Figure 7 shows the calculated total density of states (TDOS) for $TiSe_2$, VSe_2, and $V_{0.5}Ti_{0.5}Se_2$ with different ordering types (O1, O2, O3). The experimental VB spectrum for $V_{0.5}Ti_{0.5}Se_2$ is shown for comparison.

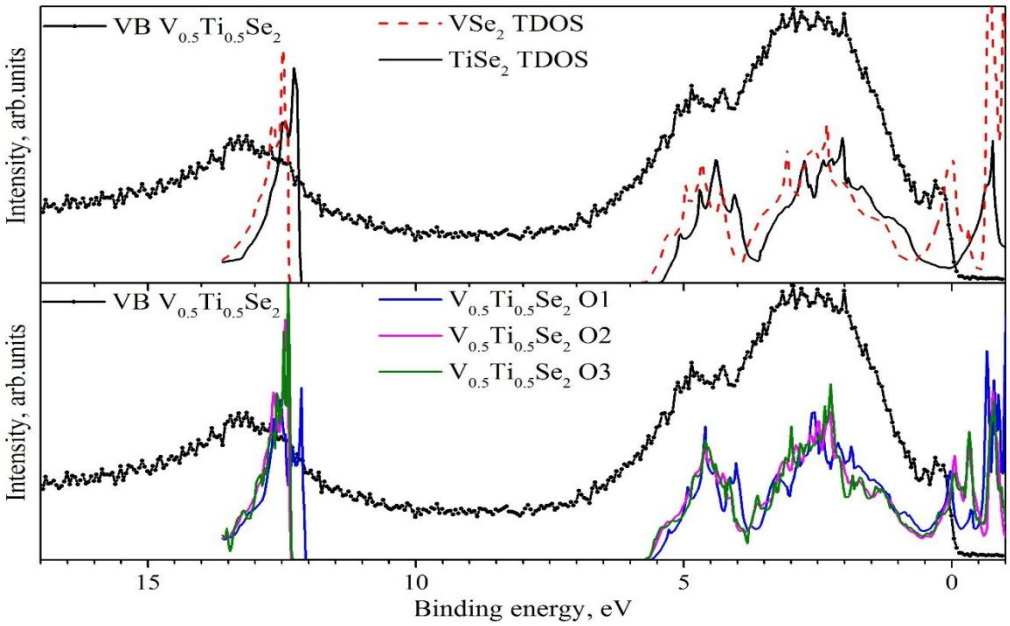

Figure 7. Valence band spectrum for $V_{0.5}Ti_{0.5}Se_2$ and calculated TDOS for $TiSe_2$ and VSe_2 (upper panel) and for $V_{0.5}Ti_{0.5}Se_2$ with different ordering types (lower panel).

One can see that only calculation for $TiSe_2$ does not describe the resonance peak at the Fermi level. The calculation for both VSe_2 and $V_{0.5}Ti_{0.5}Se_2$ describes the resonance quite well. On the other hand, the differences between the TDOS calculated for the three structural models are not significant.

Figure 8 shows Fermi surfaces calculated for $TiSe_2$, VSe_2, and $V_{0.5}Ti_{0.5}Se_2$. The cross-sections of the calculated Fermi surface were made at ¼ of the 1st Brillouin zone height (i.e., at the middle of the L-M, H-K, and Γ-A directions) using the Fermi-Surface Viewer software[51] to compare the experimental and calculation results. None of the $V_{0.5}Ti_{0.5}Se_2$ models with regular ordering between the Ti and V atoms describes the 40º angle α between the bands observed by ARPES. Therefore, we can exclude the formation of a periodically ordered substitutional $V_xT_{1-x}Se_2$ solid solution for $x \geq 0.5$. A possible explanation of the difference in the constant-energy surfaces for $V_{0.5}Ti_{0.5}Se_2$ and $V_{0.73}Ti_{0.42}Se_2$ could be the formation of $TiSe_2$ and VSe_2 structural fragments as previously suggested in reference[13]. This possibility also indicate our EMF measurements discussed in the next section.

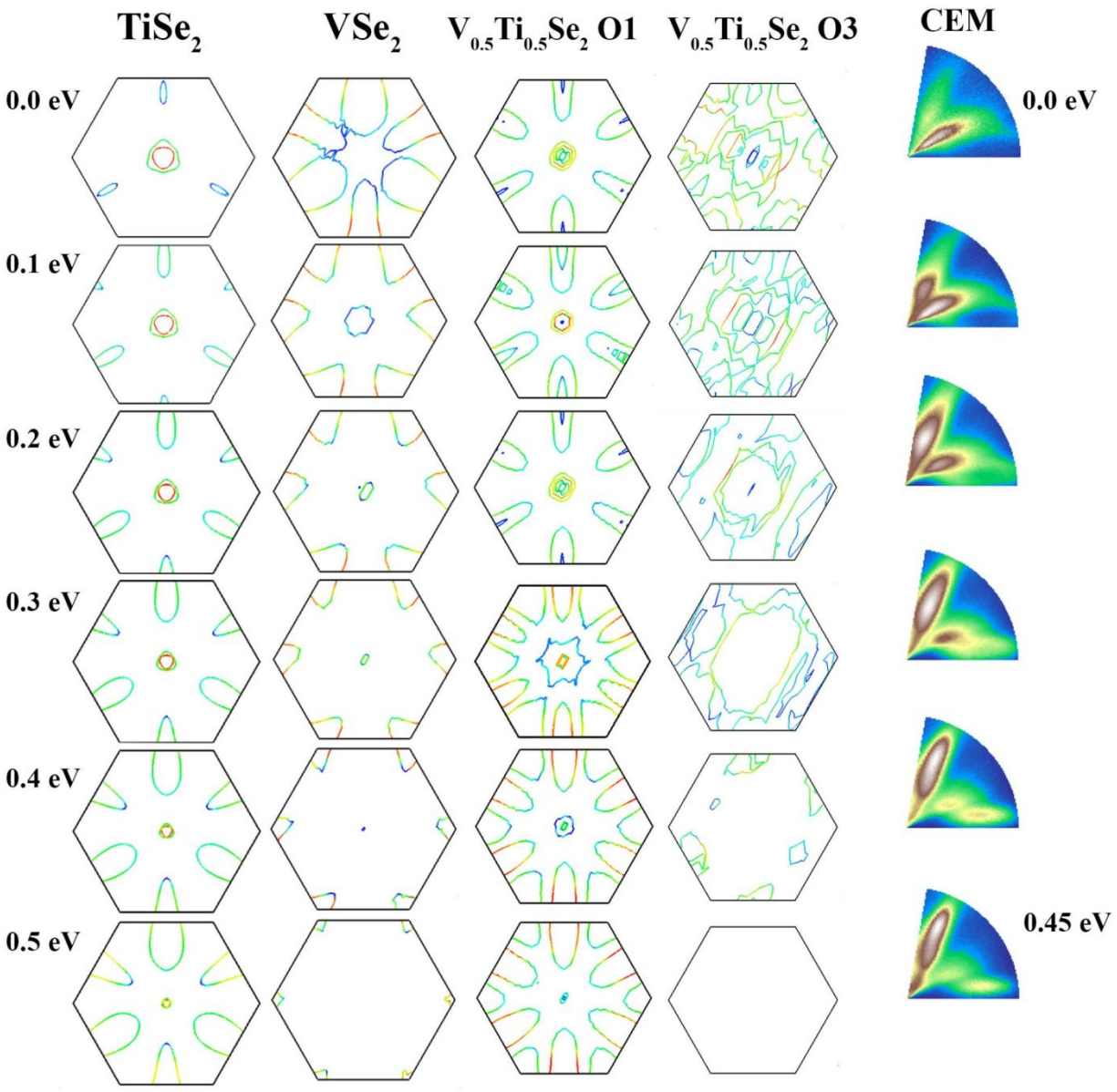

Figure 8. Calculated constant-energy maps compared with experimental data for $V_{0.5}Ti_{0.5}Se_2$.

EMF

The results of EMF measurements, which highlight changes in the electronic structure of the $V_xTi_{1-x}Se_2$ system analyzing the *E~f(x)* dependence[52,53], are shown in figure 9 .The EMF monotonically decreases with the V concentration in a range of $0 < x < 0.2$. This indicates an increase in the Fermi energy of the material. A plateau is observed in the V concentration range of $0.3 < x < 1.0$, which indicates the constancy of the Fermi energy[52–54]. The EMF also suggests that we can assume a single-phase solid solution for $x < 0.2$ and a mixture of two phases for $x > 0.3$.

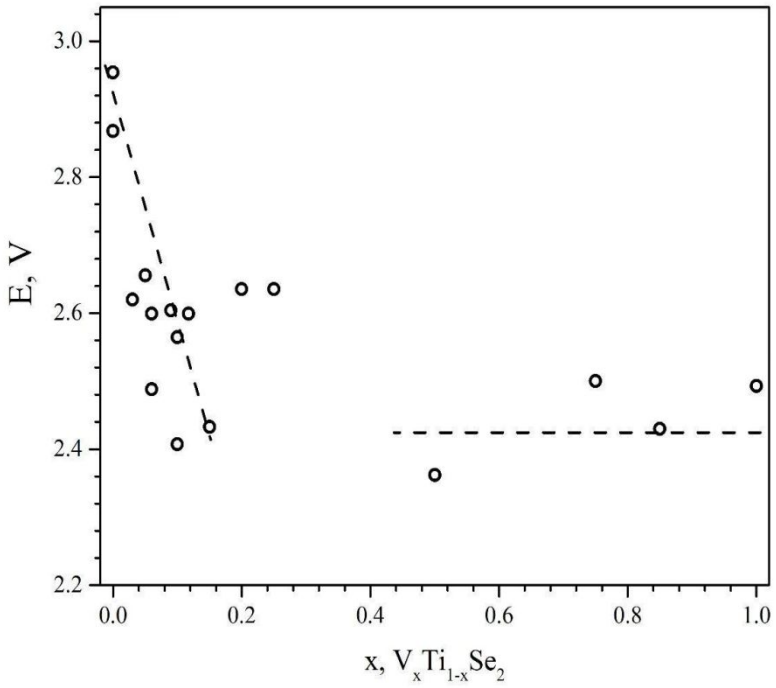

Figure 9. The EMF dependence on V concentration (x) for the $Li|Li^+|V_xTi_{1-x}Se_2$ cells at 25 °C and atmospheric pressure.

Since the chemical potential of electrons, but not atoms, is measured, only the presence of some inhomogeneities can be suggested. Although EMF method is unable to determine their real origin, phase separation could be the reason of the detected inhomogeneities. However, we can determine the $V_{0.2}Ti_{0.8}Se_2/VSe_2$ SFs ratio in $V_{0.5}Ti_{0.5}Se_2$ and $V_{0.73}Ti_{0.42}Se_2$ assuming that the change in E_F corresponds to the change in the free energy of metal in $V_xTi_{1-x}Se_2$.

AFM

We obtained the AFM images to clarify the crystal surface morphology. The AFM images of in situ cleaved $V_{0.5}Ti_{0.5}Se_2$ and $V_{0.73}Ti_{0.42}Se_2$ single crystals are shown in figure 10. For both studied single crystals, the surface is inhomogeneous and is separated into small regions. These regions are smaller in $V_{0.5}Ti_{0.5}Se_2$ than in $V_{0.73}Ti_{0.42}Se_2$, and their orientation and shapes look rather irregular; in $V_{0.73}Ti_{0.42}Se_2$, these regions look more extended and their orientation more regular.

It should be noted that both dark and light areas in figure 10, a-b correspond to flat surfaces of the crystallites. The AFM images were obtained from crystals cleaved by splitting. The cleaved surface can follow the contact border between SFs. Since the SFs are randomly distributed over the volume of the crystal and weakly bounded with each other in the direction of

the *c*-axis of the crystal, a part of them can remain on the removed part of the crystal. Therefore, the topography of the removed part can be the inverse topography of the cleaved surface. The difference in the heights between two dark areas on the opposite sides of the bright area (line profile 2 in figure 10, a) does not exceed 16 Å (see figure 10 c-d). A similar conclusion can be drawn about the difference in the heights of two bright areas separated by the dark one (direction 1 in figure 10, a). The height of the steps allows us to estimate the thickness of the SFs as ~ 15 Å, which corresponds to nearly three unit cells. Such thin crystallites will inevitably affect each other's lattice parameters. Based on the EMF results we attribute these areas to the $V_{0.2}Ti_{0.8}Se_2$ and VSe_2 SFs.

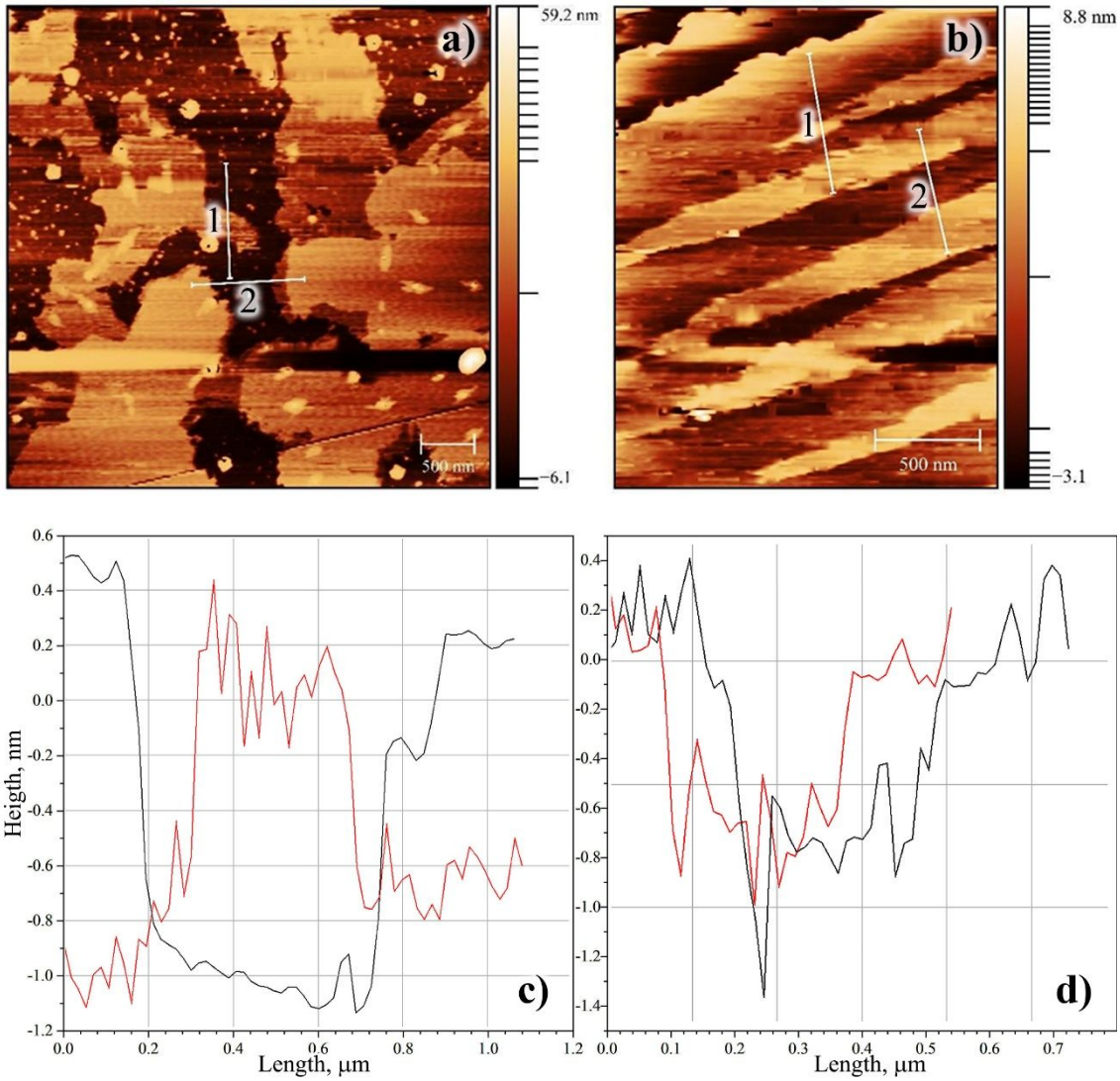

Figure 10. Panels a-b - AFM images of in situ cleaved $V_{0.5}Ti_{0.5}Se_2$ (a) and $V_{0.75}Ti_{0.42}Se_2$ (b) single crystals in height contrast. Panels c-d - line profiles along the lines 1 (red curve) and 2 (black curve) in a) and b).

The heights of the inhomogeneities, which can be attributed to the SFs, do not exceed 20 Å, while their planar size is about 1 μm. Therefore, the SFs can be described as extended thin plates with the same orientation relative to the basal plane of the crystal.

Discussion

The V 2p core level photoemission spectra (figure 2) revealed two components (A and B), which intensity ratio depends on the chemical composition (Table 1). For pure VSe_2 the peak B area/peak A area ratio equals to 0.23. For $V_xTi_{1-x}Se_2$ compounds this ratio differs from that for VSe_2. This suggests that a part of the V atoms remains in VSe_2, and another part have different chemical environment. The areas ratio enables us to estimate the relative amounts of 0.16/0.23 ≈ 0.7 for the two types of V atoms at x = 0.5. This means that in $V_{0.5}Ti_{0.5}Se_2$, 70% of V atoms are the same as in VSe_2, and 30% of V atoms are of a different type, which we attribute to the formation of $V_{0.2}Ti_{0.8}Se_2$ substitutional solid solution. The same composition of the limiting homogeneous substitution of Ti by V was obtained from the EMF measurements. Approximately the same fractions were obtained for $V_{0.73}Ti_{0.42}Se_2$. However, this material contains extra metal atoms (0.73 + 0.42 = 1.15 > 1). As reported previously,[19] V atoms occupy regular (000) sites in the host lattice, and the Ti atoms partially occupy the (00½) sites in the interlayer gap. At the same time, a change in the Ti 2p binding energy is observed only at x > 0.2. A decrease in the Ti 2p binding energy may indicate a decrease in the Ti effective charge. This cannot be explained by a shift of the Fermi level, because it is not accompanied by a corresponding decrease in the Se 3d binding energy. On the other hand, reduction of the Ti atoms is possible due to the charge transfer between the VSe_2 and $V_{0.2}Ti_{0.8}Se_2$ SFs. This is accompanied by an increase in the V 2p binding energy in $V_{0.5}Ti_{0.5}Se_2$ as compared to VSe_2. Such increase in the V 2p binding energy is masked in $V_{0.73}Ti_{0.42}Se_2$ by the extra metal atoms. The Se 3d binding energy does not depend on the V/Ti concentration ratio. This is expected for the case of SFs with the thickness close to single unit cell and the SFs are stacked on top of each other. Indeed, the AFM images on the cleaved crystals revealed terraces with a step height of ~15 Å, which corresponds to the thickness of three unit cells. Therefore, we can describe the SFs as thin layers tightly bounded to each other along the *c*-axis. This arrangement can provide a good electrical contact and charge transfer between SFs; similar lattice parameters in different SFs may be due to the mutual deformation of the SFs.

At the same time, the AFM images indicate the irregular orientation of the SFs in the basal plane in the $V_{0.5}Ti_{0.5}Se_2$ crystal and their relatively regular orientation in the $V_{0.73}Ti_{0.42}Se_2$ one. This difference in the morphology of the SFs in two crystals agrees with data obtained from the ARPES measurements. On the other hand, the LEED images for $V_{0.5}Ti_{0.5}Se_2$ and $V_{0.73}Ti_{0.42}Se_2$ crystals are typical for the crystals free of the mosaic structure. Considering the AFM data, this can be only in the case of the same [001] orientation of all the *c*-axes of the SF's.

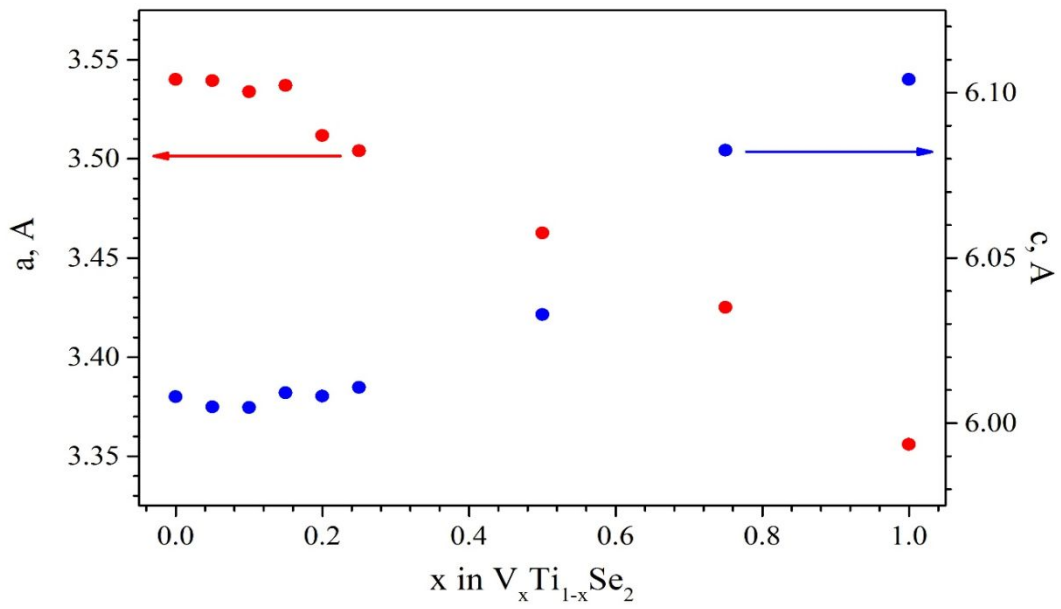

Figure 11. The V concentration dependence of the $V_xTi_{1-x}Se_2$ lattice parameters; the data were taken from Ref. [18]. The accuracy of the measurements does not exceed the symbol size.

Figure 11 shows the dependence of $V_xTi_{1-x}Se_2$ lattice parameters on V concentration. At $x < 0.2$ the lattice parameters are weakly dependent on the V concentration, however at $x > 0.2$ a linear dependence is observed. The same behavior was reported in the work of Levy and Froidevaux[16], where the special measures were taken to prevent the intercalation of Ti and/or V. Based on our XPS and EMP measurements we can conclude that in a homogeneous solid solution $V_xTi_{1-x}Se_2$ the lattice parameters do not depend on x, but they display a linear dependence on x when the material is chemically inhomogeneous. This is possible only in the case of a strong epitaxial bond between the chemically inhomogeneous layers. Surprisingly, the V concentration dependence of the lattice parameters does not deviate from the linear one even if the material is poor of Ti, and the contribution of the $V_{0.2}Ti_{0.8}Se_2$ SFs should be small. This is probably due to the large planar size of the SFs at their very small thickness. We believe that the SFs can provide a uniform deformation of the lattice even in the V concentration region close to the VSe_2 composition, where the concentration of the $V_{0.2}Ti_{0.8}Se_2$ SFs should be low.

It is obvious that the mutual effect of the SFs on the electronic and crystal structure can be achieved only in the case of their homogeneous distribution. The electrostatic interaction between the SFs caused by the charge transfer between the VSe_2 and $V_{0.2}Ti_{0.8}Se_2$ SFs can be the reason for this distribution. Since the conduction band of VSe_2 contains one electron per formula unit and that of $V_{0.2}Ti_{0.8}Se_2$ only 0.2 electrons per formula unit, one can expect a charge transfer from VSe_2 to $V_{0.2}Ti_{0.8}Se_2$. Indeed, the decrease of the Ti 2p binding energy with an increase in the V concentration in $V_xTi_{1-x}Se_2$ (figure S1) indicates this charge transfer. As a result, the VSe_2 SFs become positively charged and $V_{0.2}Ti_{0.8}Se_2$ SFs – negatively charged. The free energy of the system of electrically charged particles is minimum at their most uniform mixing and most dense mutual coordination. We believe it is the effect that is responsible for the formation of the macroscopically uniform material in the $V_xTi_{1-x}Se_2$ system.

A decrease of the Ti oxidation state in $V_{0.2}Ti_{0.8}Se_2$ at the increased concentration of VSe_2 is a side effect of the charge transfer. We have shown previously that the decrease of the Ti

oxidation state results in a similar binding energy of the octahedrally and tetrahedrally coordinated ions being intercalated into the van der Waals gap [55]. This provides a lowering of the diffusion activation energy and, therefore, an increase of the diffusion mobility of the intercalated ions, which improves the performance of the $V_xTi_{1-x}Se_2$ electrodes in contrast to the $TiSe_2$ ones, where intercalated ions occupy only the octahedral sites, and VSe_2 ones, where intercalated ions occupy only tetrahedral sites in the van der Waals gap [56].

Conclusions

In the current study, we combined XPS, ResPES, ARPES, EMF of electrochemical cells, and theoretical calculations to investigate the crystal and electronic structure of the polycrystalline $V_xTi_{1-x}Se_2$ materials and their single crystals. The results show that a homogeneous substitutional solid solution of $V_xTi_{1-x}Se_2$ is stable in the V concentration range of $0 \leq x \leq 0.2$. At $x > 0.2$ the VSe_2 structural fragments appear. The AFM microscopy and FSM analysis showed that these SFs have a shape of thin layers with a height of ~15 Å, corresponding to approximately 3 unit cells. The VSe_2 and $V_{0.2}Ti_{0.8}Se_2$ SFs are stacked to each other in the *c*-axis direction. The SFs demonstrate turbostratic disordering within the basal plane.

The contribution of the surface tension at the interfaces between SFs to the thermodynamic free energy can be much higher in 2D materials than in ordinary 3D materials. This discrepancy can lead to a redistribution of the components, which will compensate for this spatial inhomogeneity of free energy. We believe that the formation of turbostratic disordered structural fragments is expected to be a widely observed phenomenon in low-dimensional materials.

Conflicts of interest

There are no conflicts of interest to declare.

Supporting Information

The Supporting Information provides the LEED patterns for the $V_{0.5}Ti_{0.5}Se_2$ and $V_{0.73}Ti_{0.42}Se_2$single crystals, Se 3d and Ti 2p core-level XPS for $V_xTi_{1-x}Se_2$crystals taken at normal emission with $h\nu$ = 602 eV along with the energy positions of the of the Se $3d_{5/2}$ and Ti $2p_{3/2}$components, valence band spectra for $V_xTi_{1-x}Se_2$taken at normal emission with $h\nu$ = 602 eV, Ti 2p-3d and V 2p-3d ResPES for $V_{0.5}Ti_{0.5}Se_2$along with CIS spectra at E_b = 0.15 eV and difference VB spectra.

Acknowledgments

The research was carried out within the state assignment of the Ministry of Education and Science of Russia (theme “Electron” No. AAAA-A18-118020190098-5 and theme “Spin” No. AAAA-A18-118020290104-2) and with partial financial support of the RFBR (project 19-33-60031). We acknowledge Elettra Sincrotrone Trieste for providing access to its synchrotron radiation facilities. I.P., S.N., F.B., P.M.S and P.M. acknowledge funding from EUROFEL project (RoadMap Esfri).

Data availability

The data that support the findings of this study are available from the corresponding author upon reasonable request.

Bibliography

(1) Morosan, E.; Zandbergen, H. W.; Dennis, B. S.; Bos, J. W. G.; Onose, Y.; Klimczuk, T.; Ramirez, A. P.; Ong, N. P.; Cava, R. J. Superconductivity in Cu_xTiSe_2. *Nat. Phys.* **2006**, *2* (8), 544–550. https://doi.org/10.1038/nphys360.

(2) Rossnagel, K. On the Origin of Charge-Density Waves in Select Layered Transition-Metal Dichalcogenides. *J. Phys. Condens. Matter* **2011**, *23* (21), 213001. https://doi.org/10.1088/0953-8984/23/21/213001.

(3) Shkvarin, A. S.; Yarmoshenko, Y. M.; Skorikov, N. A.; Merentsov, A. I.; Titov, A. N.; Slepukhin, P. A.; Marchenko, D. E.; Sperling, M. Studying the Electronic Structure of Cr x Ti1-x Se2 by X-Ray Resonance and Absorption Spectroscopy. *J. Exp. Theor. Phys.* **2011**, *112* (1), 87–93. https://doi.org/10.1134/S1063776110061172.

(4) Titov, A. N.; Suvorova, O. N.; Ketkov, S. Y.; Titova, S. G.; Merentsov, A. I. Synthesis and Investigation of Titanium Diselenide Intercalated with Ferrocene and Cobaltocene. *Phys. Solid State* **2006**, *48* (8), 1466–1471. https://doi.org/10.1134/S1063783406080075.

(5) Thackeray, M. M.; Thomas, J. O.; Whittingham, M. S. Science and Applications of Mixed Conductors for Lithium Batteries. *MRS Bull.* **2000**, *25* (03), 39–46. https://doi.org/10.1557/mrs2000.17.

(6) Yersak, T. A.; Son, S.-B.; Cho, J. S.; Suh, S.-S.; Kim, Y.-U.; Moon, J.-T.; Oh, K. H.; Lee, S.-H. An All-Solid-State Li-Ion Battery with a Pre-Lithiated Si-Ti-Ni Alloy Anode. *J. Electrochem. Soc.* **2013**, *160* (9), A1497–A1501. https://doi.org/10.1149/2.086309jes.

(7) Trevey, J. E.; Stoldt, C. R.; Lee, S.-H. High Power Nanocomposite TiS2 Cathodes for All-Solid-State Lithium Batteries. *J. Electrochem. Soc.* **2011**, *158* (12), A1282. https://doi.org/10.1149/2.017112jes.

(8) Hu, S.; Wang, X. Ultrathin Nanostructures: Smaller Size with New Phenomena. *Chem. Soc. Rev.* **2013**, *42* (12), 5577. https://doi.org/10.1039/c3cs00006k.

(9) Shin, B. R.; Nam, Y. J.; Kim, J. W.; Lee, Y.-G.; Jung, Y. S. Interfacial Architecture for Extra Li+ Storage in All-Solid-State Lithium Batteries. *Sci. Rep.* **2014**, *4,* 5572. https://doi.org/10.1038/srep05572.

(10) Elazari, R.; Salitra, G.; Gershinsky, G.; Garsuch, A.; Panchenko, A.; Aurbach, D. Li Ion Cells Comprising Lithiated Columnar Silicon Film Anodes, TiS2 Cathodes and Fluoroethyene Carbonate (FEC) as a Critically Important Component. *J. Electrochem. Soc.* **2012**, *159* (9), A1440–A1445. https://doi.org/10.1149/2.029209jes.

(11) Clark, S. J.; Wang, D.; Armstrong, A. R.; Bruce, P. G. Li(V0.5Ti0.5)S2 as a 1 V Lithium Intercalation Electrode. *Nat. Commun.* **2016**, *7* (1), 10898. https://doi.org/10.1038/ncomms10898.

(12) Tarascon, J. M.; DiSalvo, F. J.; Eibschutz, M.; Murphy, D. W.; Waszczak, J. V. Preparation and Chemical and Physical Properties of the New Layered Phases LixTi1−yMyS2 with M=V, Cr, or Fe. *Phys. Rev. B* **1983**, *28* (11), 6397–6406. https://doi.org/10.1103/PhysRevB.28.6397.

(13) Merentsov, A. I.; Shkvarin, A. S.; Postnikov, M. S.; Gregoratti, L.; Amati, M.; Zeller, P.; Moras, P.; Titov, A. N. Studying the Heterogeneity of the CrxTi1-XCh2 (Ch = S, Se) Single Crystals Using X-Ray Scanning Photoemission Microscopy. *J. Phys. Chem. Solids* **2022**, *160*, 110309. https://doi.org/10.1016/j.jpcs.2021.110309.

(14) Titov, A. N.; Shkvarin, A. S.; Merentsov, A. I.; Bushkova, O. V.; Suslov, E. A.; Titov, A. A.; Avila, J.; Asensio, M. C.; Kazantseva, N. V.; Postnikov, M. S. Janus Layers in the

TiSe 2 –TiS 2 System. *Chem. Mater.* **2021**, *33* (22), 8915–8925. https://doi.org/10.1021/acs.chemmater.1c03232.

(15) Brezhestovskii, M. S.; Suslov, E. A.; Bushkova, O. V.; Merentsov, A. I.; Titov, A. N. Influence of Heterovalent Substitution in the Titanium Sublattice on the Electrochemical Intercalation of Lithium in M y Ti1–y Se2 (M = Cr, V)). *Phys. Solid State* **2015**, *57* (10), 2078–2086.

(16) Levy, F.; Froidevaux, Y. Structural and Electrical Properties of Layered Transition Metal Selenides VxTi1-XSe2 and TaxTi1-XSe2. *J. Phys. C Solid State Phys.* **1979**, *12* (3), 473. https://doi.org/10.1088/0022-3719/12/3/015.

(17) Di Salvo, F. J.; Waszczak, J. V. Transport Properties and the Phase Transition in Ti1−xMxSe2 (M=Ta or V). *Phys. Rev. B* **1978**, *17* (10), 3801–3807. https://doi.org/10.1103/PhysRevB.17.3801.

(18) Shkvarin, A. S.; Merentsov, A. I.; Yarmoshenko, Y. M.; Shkvarina, E. G.; Zhukov, Y. M.; Titov, A. A.; Titov, A. N. Electronic Structure of V x Ti 1−x Se 2 in Wide Concentration Region ($0.06 \leq x \leq 0.9$). *J. Chem. Phys.* **2017**, *146* (16), 164703. https://doi.org/10.1063/1.4981522.

(19) Shkvarin, A. S.; Yarmoshenko, Y. M.; Merentsov, A. I.; Shkvarina, E. G.; Gubkin, A. F.; Píš, I.; Nappini, S.; Bondino, F.; Bobrikov, I. A.; Titov, A. N. Electronic Structures of the Vanadium-Intercalated and Substitutionally Doped Transition-Metal Dichalcogenides $Ti_xV_ySe_2$. *Inorg. Chem.* **2020**, *59* (12), 8543–8551. https://doi.org/10.1021/acs.inorgchem.0c00953.

(20) Di Salvo, F. J.; Moncton, D. E.; Waszczak, J. V. Electronic Properties and Superlattice Formation in the Semimetal TiSe2. *Phys. Rev. B* **1976**, *14* (10), 4321–4328. https://doi.org/10.1103/PhysRevB.14.4321.

(21) Cercellier, H.; Monney, C.; Clerc, F.; Battaglia, C.; Despont, L.; Garnier, M. G.; Beck, H.; Aebi, P.; Patthey, L.; Berger, H. et al. Evidence for an Excitonic Insulator Phase in 1T−TiSe2. *Phys. Rev. Lett.* **2007**, *99* (14), 146403. https://doi.org/10.1103/PhysRevLett.99.146403.

(22) Liu, J.; Hou, W.-J.; Cheng, C.; Fu, H.-X.; Sun, J.-T.; Meng, S. Intrinsic Valley Polarization of Magnetic VSe 2 Monolayers. *J. Phys. Condens. Matter* **2017**, *29* (25), 255501. https://doi.org/10.1088/1361-648X/aa6e6e.

(23) Rossnagel, K.; Kipp, L.; Skibowski, M. Charge-Density-Wave Phase Transition in 1T−$TiSe_2$: Excitonic Insulator versus Band-Type Jahn-Teller Mechanism. *Phys. Rev. B* **2002**, *65* (23), 235101. https://doi.org/10.1103/PhysRevB.65.235101.

(24) Joe, Y. I.; Chen, X. M.; Ghaemi, P.; Finkelstein, K. D.; de la Peña, G. A.; Gan, Y.; Lee, J. C. T.; Yuan, S.; Geck, J.; MacDougall, G. J. et al. Emergence of Charge Density Wave Domain Walls above the Superconducting Dome in 1T-TiSe 2. *Nat. Phys.* **2014**, *10* (6), 421–425. https://doi.org/10.1038/nphys2935.

(25) Hellgren, M.; Baima, J.; Bianco, R.; Calandra, M.; Mauri, F.; Wirtz, L. Critical Role of the Exchange Interaction for the Electronic Structure and Charge-Density-Wave Formation in TiSe2. *Phys. Rev. Lett.* **2017**, *119* (17), 176401. https://doi.org/10.1103/PhysRevLett.119.176401.

(26) van Bruggen, C. F.; Haas, C. Magnetic Susceptibility and Electrical Properties of VSe2 Single Crystals. *Solid State Commun.* **1976**, *20* (3), 251–254. https://doi.org/10.1016/0038-1098(76)90187-3.

(27) Whittingham, M. S. The Electrochemical Characteristics of VSe2 in Lithium Cells. *Mater. Res. Bull.* **1978**, *13* (9), 959–965. https://doi.org/10.1016/0025-5408(78)90108-3.

(28) Hughes, H. P.; Webb, C.; Williams, P. M. Angle Resolved Photoemission from VSe 2. *J. Phys. C Solid State Phys.* **1980**, *13* (6), 1125–1138. https://doi.org/10.1088/0022-3719/13/6/022.

(29) Li, F.; Tu, K.; Chen, Z. Versatile Electronic Properties of VSe 2 Bulk, Few-Layers, Monolayer, Nanoribbons, and Nanotubes: A Computational Exploration. *J. Phys. Chem. C* **2014**, *118* (36), 21264–21274. https://doi.org/10.1021/jp507093t.

(30) Pásztor, Á.; Scarfato, A.; Barreteau, C.; Giannini, E.; Renner, C. Dimensional Crossover of the Charge Density Wave Transition in Thin Exfoliated VSe 2. *2D Mater.* **2017**, *4* (4), 041005. https://doi.org/10.1088/2053-1583/aa86de.

(31) Rimmington, H. P. B.; Balchin, A. A.; Tanner, B. K. Nearly Perfect Single Crystals of Layer Compounds Grown by Iodine Vapour-Transport Techniques. *J. Cryst. Growth* **1972**, *15* (1), 51–56. https://doi.org/10.1016/0022-0248(72)90319-3.

(32) Rouxel, J. Structural Chemistry of Layered Materials and Their Intercalates. *Phys. B+C* **1980**, *99* (1–4), 3–11. https://doi.org/10.1016/0378-4363(80)90203-X.

(33) Friend, R. H.; Yoffe, A. D. Electronic Properties of Intercalation Complexes of the Transition Metal Dichalcogenides. *Adv. Phys.* **1987**, *36* (1), 1–94. https://doi.org/10.1080/00018738700101951.

(34) Wiegers, G. A. The Characterisation of VSe 2 : A Study of the Thermal Expansion. *J. Phys. C Solid State Phys.* **1981**, *14* (29), 4225–4235. https://doi.org/10.1088/0022-3719/14/29/010.

(35) Fu, J.; Ali, R.; Mu, C.; Liu, Y.; Mahmood, N.; Lau, W.-M.; Jian, X. Large-Scale Preparation of 2D VSe2 through a Defect-Engineering Approach for Efficient Hydrogen Evolution Reaction. *Chem. Eng. J.* **2021**, *411*, 128494. https://doi.org/10.1016/j.cej.2021.128494.

(36) Zelenina, L. N.; Chusova, T. P.; Titov, A. N. Thermodynamic Properties of Titanium Selenides with Variable Composition TiSe2-TiSe1.80. *Russ. Chem. Bull.* **2011**, *60* (3), 581–584. https://doi.org/10.1007/s11172-011-0089-8.

(37) Shkvarin, A. S.; Yarmoshenko, Y. M.; Skorikov, N. A.; Yablonskikh, M. V.; Merentsov, A. I.; Shkvarina, E. G.; Titov, A. N. Electronic Structure of Titanium Dichalcogenides TiX 2 (X = S, Se, Te). *J. Exp. Theor. Phys.* **2012**, *114* (1), 150–156. https://doi.org/10.1134/S1063776112010177.

(38) Shkvarina, E. G.; Titova, S. G.; Titov, A. N.; Shkvarin, A. S. The Mechanism of the Formation of One-Dimensional Chains of the Iron and Vanadium Atoms in the TiSe 2 Interlayer Space. *J. Alloys Compd.* **2017**, *717*, 286–293. https://doi.org/10.1016/j.jallcom.2017.05.078.

(39) Zangrando, M.; Finazzi, M.; Paolucci, G.; Comelli, G.; Diviacco, B.; Walker, R. P.; Cocco, D.; Parmigiani, F. BACH, the Beamline for Advanced Dichroic and Scattering Experiments at ELETTRA. *Rev. Sci. Instrum.* **2001**, *72* (2), 1313. https://doi.org/10.1063/1.1334626.

(40) Cui, X. Y.; Negishi, H.; Titova, S. G.; Shimada, K.; Ohnishi, A.; Higashiguchi, M.; Miura, Y.; Hino, S.; Jahir, A. M.; Titov, A. et al. Direct Evidence of Band Modification and Suppression of Superstructure in TiSe2 upon Fe Intercalation: An Angle-Resolved

Photoemission Study. *Phys. Rev. B* **2006**, *73* (8), 085111. https://doi.org/10.1103/PhysRevB.73.085111.

(41) Perdew, J. P.; Burke, K.; Ernzerhof, M. Generalized Gradient Approximation Made Simple. *Phys. Rev. Lett.* **1996**, *77* (18), 3865–3868. https://doi.org/10.1103/PhysRevLett.77.3865.

(42) ELK – open access code: http://elk.sourceforge.net/ (accessed Apr 1, 2022).

(43) Bachrach, R. Z. *Synchrotron Radiation Research Advances in Surface and Interface Science*; Bachrach, R. Z., Ed.; Springer US: Boston, MA, 1992; Vol. 1. https://doi.org/10.1007/978-1-4615-3278-1.

(44) Kay, A.; Arenholz, E.; Mun, S.; Abajo, F. J. G. de; Fadley, C. S.; Denecke, R.; Hussain, Z.; Hove, M. A. Van. Multi-Atom Resonant Photoemission: A Method for Determining Near-Neighbor Atomic Identities and Bonding. *Science (80-.).* **1998**, *281* (5377), 679–683. https://doi.org/10.1126/science.281.5377.679.

(45) Rubensson, J.-E.; Lüning, J.; Eisebitt, S.; Eberhardt, W. It's Always a One-Step Process. *Appl. Phys. A Mater. Sci. Process.* **1997**, *65* (2), 91–96. https://doi.org/10.1007/s003390050549.

(46) Mårtensson, N.; Weinelt, M.; Karis, O.; Magnuson, M.; Wassdahl, N.; Nilsson, A.; Stöhr, J.; Samant, M. Coherent and Incoherent Processes in Resonant Photoemission. *Appl. Phys. A Mater. Sci. Process.* **1997**, *65* (2), 159–167. https://doi.org/10.1007/s003390050559.

(47) Hüfner, S.; Yang, S.-H.; Mun, B. S.; Fadley, C. S.; Schäfer, J.; Rotenberg, E.; Kevan, S. D. Observation of the Two-Hole Satellite in Cr and Fe Metal by Resonant Photoemission at the 2p Absorption Energy. *Phys. Rev. B* **2000**, *61* (19), 12582–12585. https://doi.org/10.1103/PhysRevB.61.12582.

(48) Strocov, V. N.; Shi, M.; Kobayashi, M.; Monney, C.; Wang, X.; Krempasky, J.; Schmitt, T.; Patthey, L.; Berger, H.; Blaha, P. Three-Dimensional Electron Realm in VSe2 by Soft-X-Ray Photoelectron Spectroscopy: Origin of Charge-Density Waves. *Phys. Rev. Lett.* **2012**, *109* (8), 086401. https://doi.org/10.1103/PhysRevLett.109.086401.

(49) Pillo, T.; Hayoz, J.; Berger, H.; Lévy, F.; Schlapbach, L.; Aebi, P. Photoemission of Bands above the Fermi Level: The Excitonic Insulator Phase Transition in 1T−TiSe2. *Phys. Rev. B* **2000**, *61* (23), 16213–16222. https://doi.org/10.1103/PhysRevB.61.16213.

(50) Feng, J.; Biswas, D.; Rajan, A.; Watson, M. D.; Mazzola, F.; Clark, O. J.; Underwood, K.; Marković, I.; McLaren, M.; Hunter, A. et al. Electronic Structure and Enhanced Charge-Density Wave Order of Monolayer VSe 2. *Nano Lett.* **2018**, *18* (7), 4493–4499. https://doi.org/10.1021/acs.nanolett.8b01649.

(51) Kawamura, M. FermiSurfer: Fermi-Surface Viewer Providing Multiple Representation Schemes. *Comput. Phys. Commun.* **2019**, *239*, 197–203. https://doi.org/10.1016/j.cpc.2019.01.017.

(52) Shkvarin, A. S.; Yarmoshenko, Y. M.; Merentsov, A. I.; Shkvarina, E. G.; Suslov, E. A.; Brezhestovsky, M. S.; Bushkova, O. V.; Titov, A. N. Chemical Bond in FexTiSe2 Intercalation Compounds: Dramatic Influence of Fe Concentration. *RSC Adv.* **2016**, *6* (108), 106527–106539. https://doi.org/10.1039/c6ra16857d.

(53) Suslov, E. A.; Doroshek, A. A.; Titov, A. A.; Titov, A. N. Determination of the Critical Points for Intercalating Systems by the EMF Method Concerning Foreign Metal. *J. Phys. Chem. A* **2021**, *125* (9), 1981–1986. https://doi.org/10.1021/acs.jpca.0c08998.

(54) MOLENDA, J. Electronic Limitations of Lithium Diffusibility. From Layered and Spinel toward Novel Olivine Type Cathode Materials. *Solid State Ionics* **2005**, *176* (19–22), 1687–1694. https://doi.org/10.1016/j.ssi.2005.04.018.

(55) Shkvarina, E. G.; Merentsov, A. I.; Postnikov, M. S.; Shkvarin, A. S.; Pryanichnikov, S. V.; Píš, I.; Nappini, S.; Bondino, F.; Titov, A. N. Electronic and Crystal Structure of Bi-Intercalated Titanium Diselenide Cu x Ni y TiSe 2. *J. Mater. Chem. C* **2021**, *9* (5), 1657–1670. https://doi.org/10.1039/D0TC03277H.

(56) Murphy, D. W.; Di Salvo, F. J.; Hull, G. W.; Waszczak, J. V. Convenient Preparation and Physical Properties of Lithium Intercalation Compounds of Group 4B and 5B Layered Transition Metal Dichalcogenides. *Inorg. Chem.* **1976**, *15* (1), 17–21. https://doi.org/10.1021/ic50155a005.

TOC Graphic

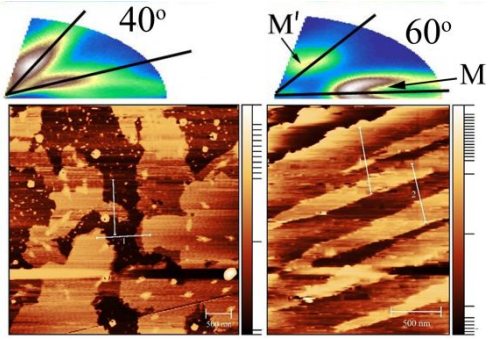

Supporting Information

Electronic Structure of $V_xTi_{1-x}Se_2$ Solid Solutions with the $(V,Ti)Se_2$ Structural Fragments

Shkvarin A.S.[1*], Merentsov A.I.[1], Postnikov M.S.[1], Yarmoshenko Yu.M.[1], Shkvarina E.G.[1], Suslov E.A.[1], Kuznetsova A.Yu.[1,2], Píš I.[3,4], Nappini S.[4], Bondino F.[4], Moras P.[5], Sheverdyaeva P.M.[5], Betz-Guttner E.[4], TitovA.N.[1,2]

[1]M.N. Miheev Institute of Metal Physics of Ural Branch of Russian Academy of Sciences, 620990 Ekaterinburg, Russia

[2]Ural FederalUniversity, 620089 Ekaterinburg, Russia

[3]Elettra-Sincrotrone Trieste S.C.p.A, S.S. 14, km 163.5, 34149 Basovizza (TS), Italy

[4]IOM-CNR, Laboratorio TASC, S.S. 14-km 163.5, 34149 Basovizza, Trieste, Italy

[5]Istituto di Struttura della Materia-CNR (ISM-CNR), SS 14, Km 163,5, 34149, Trieste, Italy

*Email: shkvarin@imp.uran.ru

The LEED patterns were captured from the cleaved surface of the crystals in the preparation chamber of the spectrometer at the VUV Photoemission beamline of the ELETTRA sinchrotrone facility.

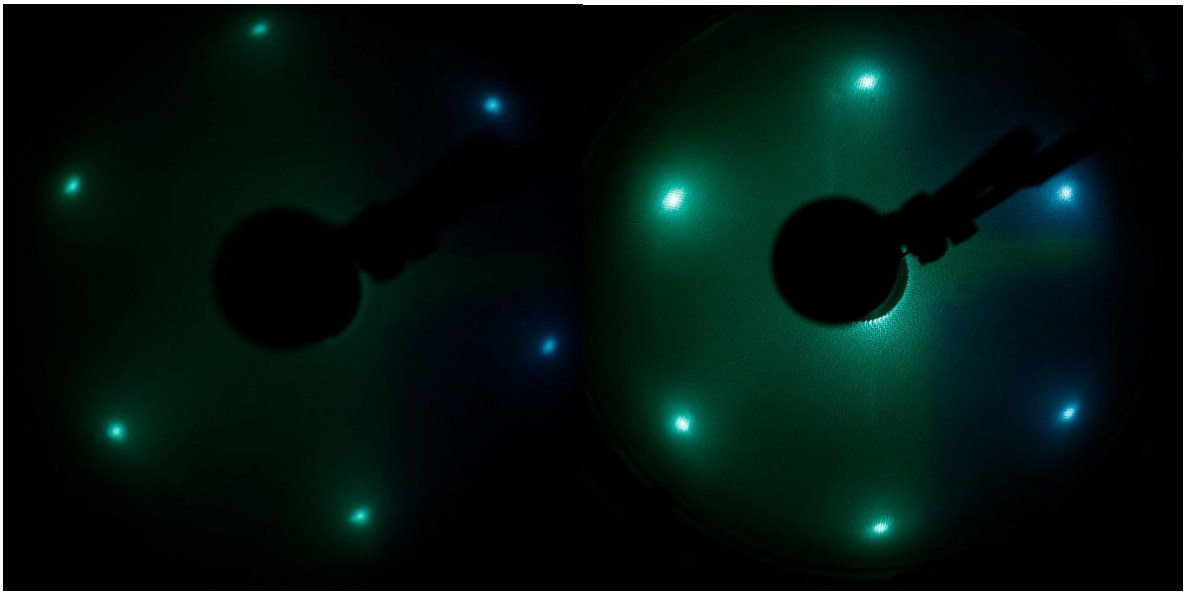

Figure S0. LEED patterns for the $V_{0.5}Ti_{0.5}Se_2$ and $V_{0.73}Ti_{0.42}Se_2$ single crystals.

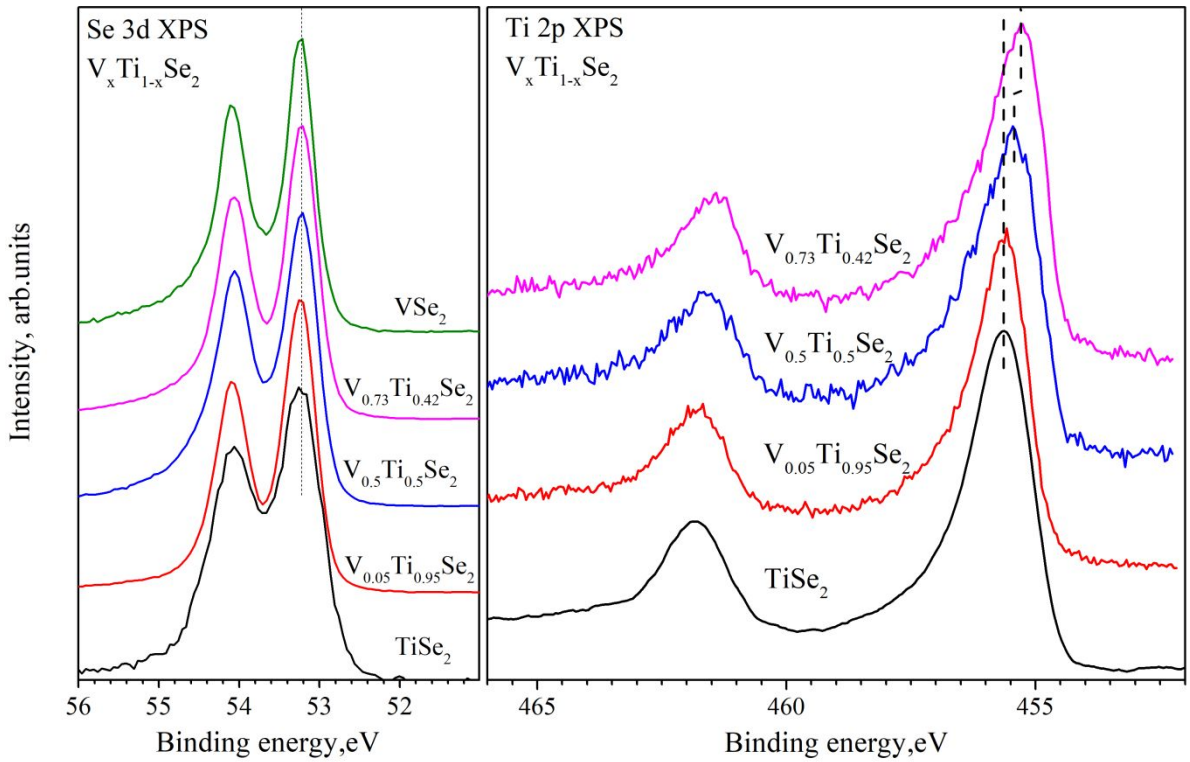

Figure S1. Left panel: XPS Se 3d core level for $V_xTi_{1-x}Se_2$. Right panel: XPS Ti 2p core level for $V_xTi_{1-x}Se_2$. All spectra were taken at normal emission with $h\nu$ = 602 eV.

Table S1. The Se $3d_{5/2}$ and Ti $2p_{3/2}$ energy positions of the spectra displayed in figure S1.

Sample	Se $3d_{5/2}$	Ti $2p_{3/2}$
$TiSe_2$	53.24	455.67
$V_{0.05}Ti_{0.95}Se_2$	53.24	455.6
$V_{0.5}Ti_{0.5}Se_2$	53.24	455.46
$V_{0.73}Ti_{0.42}Se_2$	53.24	455.29
VSe_2	53.24	-

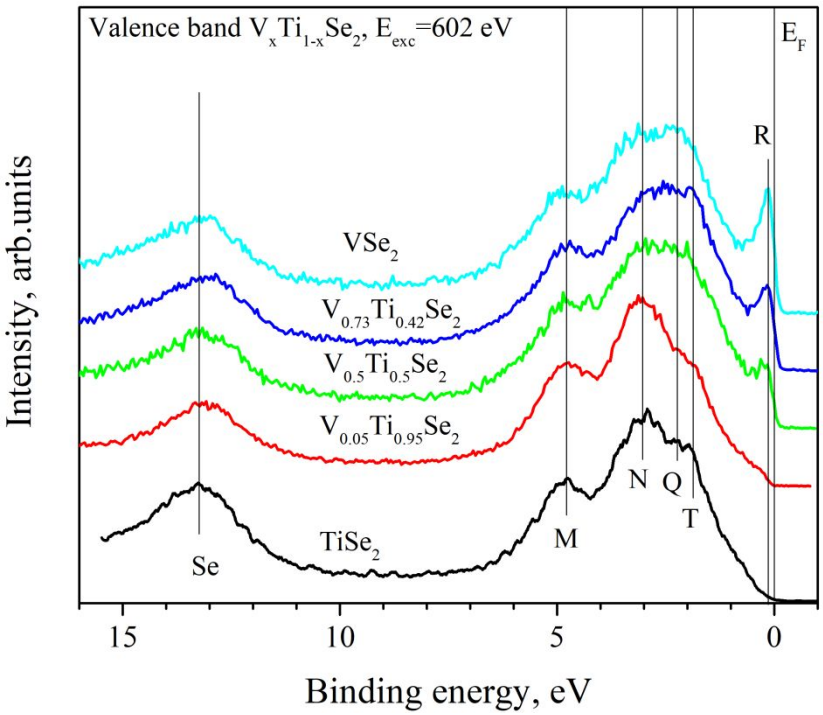

Figure S2. Valence band spectra for $V_xTi_{1-x}Se_2$ taken at normal emission with $h\nu$ = 602 eV.

Ti and V $L_{2,3}$ XAS were performed in total electron yield mode by measuring the drain current through the sample. The photon energy resolution was set to 0.1 eV at Ti L-edge and 0.15 eV at V L-edge, respectively.

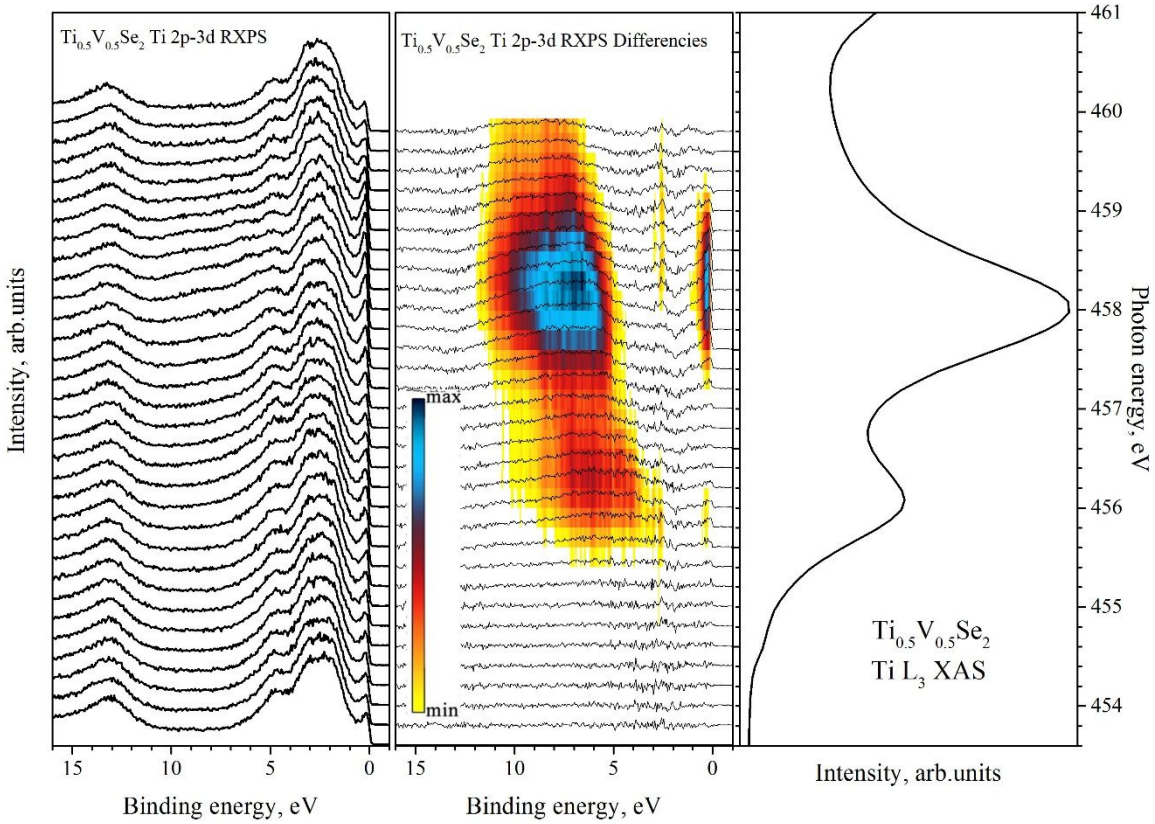

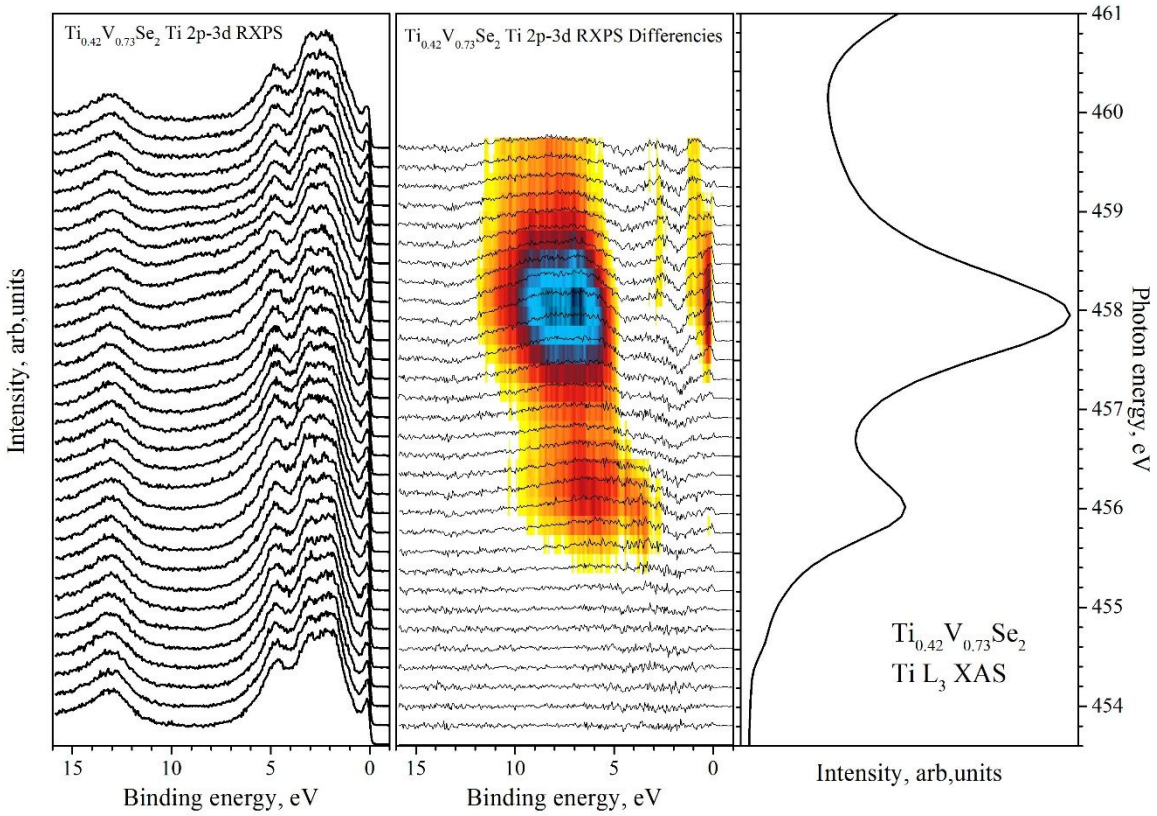

Figure S3. Upper panel: Ti 2p–3d ResPES for $Ti_{0.5}V_{0.5}Se_2$. Lower panel: Ti 2p–3d ResPES for $Ti_{0.42}V_{0.73}Se_2$. In the middle of both panel the difference spectra are shown in the form of an image plot.

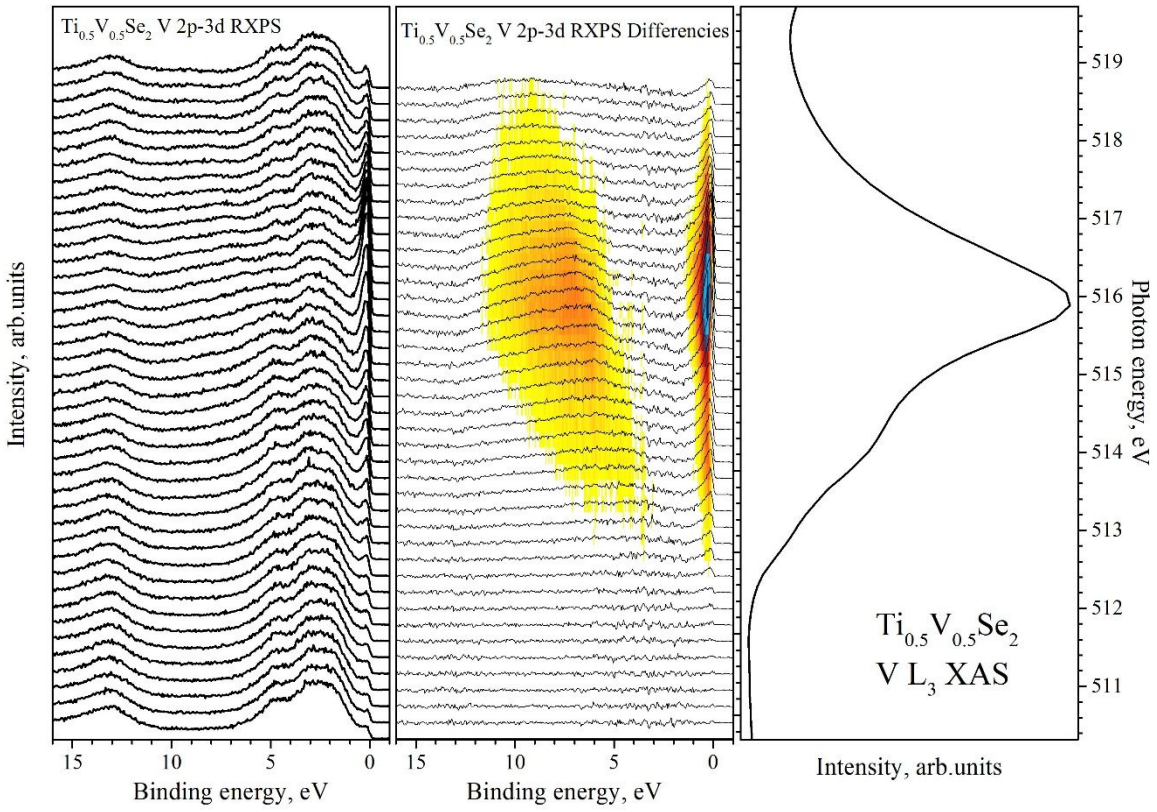

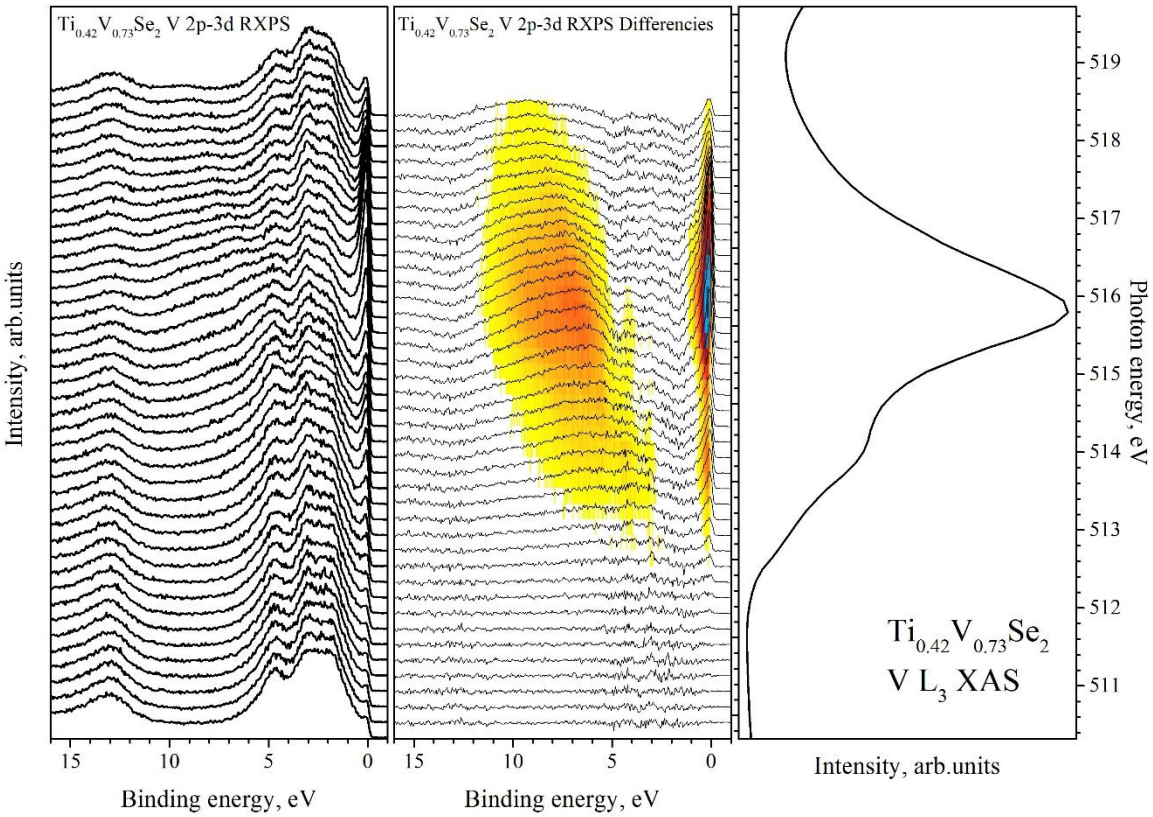

Figure S4. Upper panel: V 2p–3d ResPES for $Ti_{0.5}V_{0.5}Se_2$. Lower panel: V 2p–3d ResPES for $Ti_{0.42}V_{0.73}Se_2$. In the middle of both panel the difference spectra are shown in the form of an image plot.

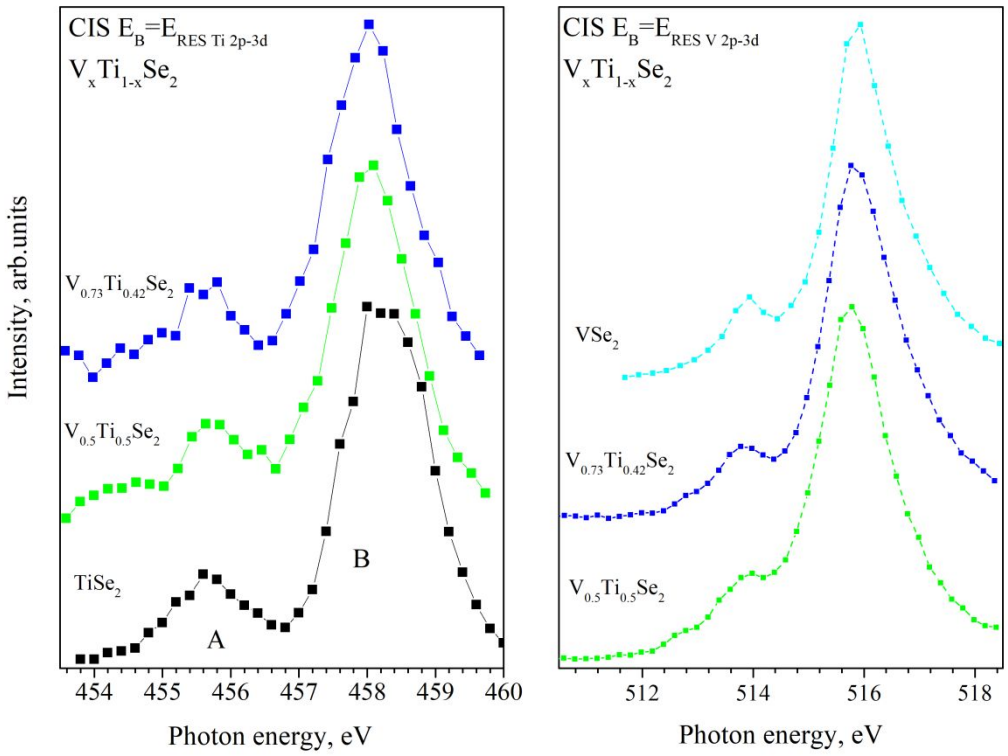

Figure S5. CIS spectra at E_b = 0.15 eV, obtained from the Ti 2p-3d (left panel) and V 2p-3d (right panel) ResPES spectra.

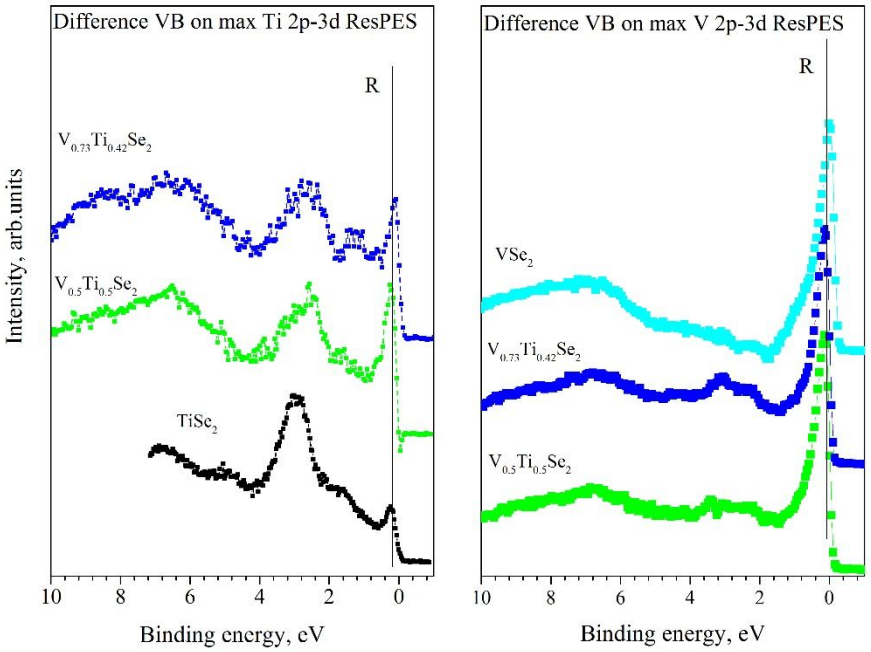

Figure S6. Difference VB spectra for $V_xTi_{1-x}Se_2$ obtained from the Ti 2p-3d (left panel) and V 2p-3d (right panel) ResPES spectra.